

SUPERBURST MODELS FOR NEUTRON STARS WITH HYDROGEN AND HELIUM-RICH ATMOSPHERES

L. KEEK

National Superconducting Cyclotron Laboratory, Department of Physics and Astronomy, and Joint Institute for Nuclear Astrophysics,
Michigan State University, East Lansing, MI 48824, USA

A. HEGER

School of Physics and Astronomy, University of Minnesota, 116 Church Street SE, Minneapolis, MN 55455, USA

J. J. M. IN 'T ZAND

SRON Netherlands Institute for Space Research, Sorbonnelaan 2, 3584 CA Utrecht, The Netherlands

Abstract

Superbursts are rare day-long Type I X-ray bursts due to carbon flashes on accreting neutron stars in low-mass X-ray binaries. They heat the neutron star envelope such that the burning of accreted hydrogen and helium becomes stable, and the common shorter X-ray bursts are quenched. Short bursts reappear only after the envelope cools down. We study multi-zone one-dimensional models of the neutron star envelope, in which we follow carbon burning during the superburst, and we include hydrogen and helium burning in the atmosphere above. We investigate both the case of a solar composition and a helium-rich atmosphere. This allows us to study for the first time a wide variety of thermonuclear burning behavior as well as the transitions between the different regimes in a self-consistent manner. For solar composition, burst quenching ends much sooner than previously expected. This is because of the complex interplay between the 3α , hot CNO, and CNO breakout reactions. Stable burning of hydrogen and helium transitions via marginally stable burning (mHz quasi-periodic oscillations) to less energetic bursts with short recurrence times. We find a short-lived bursting mode where weaker and stronger bursts alternate. Eventually the bursting behavior changes back to that of the pre-superburst bursts. Because of the scarcity of observations, this transition has not been directly detected after a superburst. Using the MINBAR burst catalog we identify the shortest upper limit on the quenching time for 4U 1636–536, and derive further constraints on the time scale on which bursts return.

Subject headings: accretion, accretion disks — methods: numerical — nuclear reactions, nucleosynthesis, abundances — stars: neutron — X-rays: binaries — X-rays: bursts

1. INTRODUCTION

Superbursts are day-long flares observed from neutron stars in low-mass X-ray binaries (LMXBs; Cornelisse et al. 2000; Strohmayer & Brown 2002), that are attributed to the unstable thermonuclear burning of a carbon-rich layer (Cumming & Bildsten 2001; see Cooper et al. 2009 for a discussion on alternative types of fuel). The thermonuclear runaway starts at a column depth of $y = 10^{11} \text{ g cm}^{-2}$ to $y = 10^{12} \text{ g cm}^{-2}$, close to the outer crust (Cumming et al. 2006). Because of the high temperature dependence of carbon burning (e.g., Caughlan & Fowler 1988), the ignition is sensitive to crustal heating, and hence superburst observations place constraints on the combined crustal heating and neutrino cooling of the crust and core. For example, the superburst from the classical transient X-ray source 4U 1608–522 requires the crust to have heated up faster than predicted by current models (Keek et al. 2008). Because of the long typical recurrence time of approximately a year, superbursts are rare: so far 22 (candidates) have been detected from 13 sources (e.g., Keek & in 't Zand 2008; see Kuulkers 2009; Chenevez et al. 2011; in 't Zand et al. 2011; Serino et al. 2012; Asada et al. 2011 for recent discoveries; see also Table 2).

The carbon fuel is expected to be produced by thermonuclear burning of accreted hydrogen and/or helium higher up in the atmosphere (e.g., Strohmayer & Brown 2002). All known superbursting sources exhibit unstable hydrogen/helium burning observed as short (up to $\sim 100 \text{ s}$ duration) Type I X-ray bursts, as well as stable burning, evidenced by high values of the α parameter, the ratio of the integrated persistent emission between two bursts and the burst fluence (in 't Zand et al. 2003). This burning takes place at a column depth of $y \simeq 10^8 \text{ g cm}^{-2}$. Whereas stable hydrogen/helium burning through the hot CNO cycle and the 3α -process produce carbon, it is destroyed in bursts by CNO-cycle breakout reactions, followed by a series of helium captures catalyzed by protons — the αp -process — and proton captures with subsequent β decays — the rp -process — creating heavier elements (Schatz et al. 2001, 2003). Current models produce burst ashes with a carbon mass fraction of typically 5% (Woosley et al. 2004), whereas a slightly higher mass fraction is found for models that accrete material with a higher metallicity at a lower rate. Superburst observations, however, indicate a carbon content that is closer to 20% (Cumming et al. 2006). Medin & Cumming (2011) recently suggested that chemical separation by freeze out close to the outer crust may increase the carbon fraction.

If the superburst ignites in a sufficiently thick layer, carbon burning initially proceeds as a detonation (Weinberg et al. 2006). This produces a shock that travels to the surface, pushing the envelope outward. The hydrogen/helium-rich atmosphere is heated by the shock (Weinberg & Bildsten 2007) and the subsequent fall-back of the outer layers (Keek & Heger 2011). This produces a bright precursor burst. Furthermore, the ignition conditions for a hydrogen/helium flash are reached. X-ray emission from this flash adds to the precursor burst, or it may account for the entire precursor emission, in case there is no strong shock (Keek & Heger 2011). Precursor bursts have been identified in all cases when the start of the superburst was observed and the data were of sufficient quality (e.g., Kuulkers 2004).

After the precursor burst, the envelope is sufficiently hot for all subsequently accreted hydrogen and helium to burn stably at the same rate at which it is accreted: the bursts are quenched (Cornelisse et al. 2000; Cumming & Bildsten 2001; Kuulkers et al. 2002). After the envelope has cooled down, unstable burning resumes, and Type I bursts return. Quenching times of one to several weeks are predicted (Cumming & Macbeth 2004). Because of non-contiguous observing schedules and the presence of frequent data gaps due to Earth occultations and South Atlantic Anomaly passages, the end of the quenching period and the reappearance of bursts have most likely not been observed. Only upper limits of more than one month have been derived for the quenching time (e.g., Kuulkers 2004).

The return of hydrogen/helium bursts after a superburst provides a unique opportunity to study the transition of stable to unstable burning in the neutron star atmosphere. This transition is observed in a number of LMXBs, and is associated with changes in the mass accretion rate (e.g., Cornelisse et al. 2003). A higher rate implies a hotter envelope as well as a faster accumulation of accreted material, which leads to steady-state burning of hydrogen and helium. Current burst models predict that this transition occurs at a 10 times higher accretion rate than inferred from observations (e.g., Heger et al. 2007b), although increased crustal heating (e.g., Gupta et al. 2007) and rotationally induced turbulent mixing (Piro & Bildsten 2007) may reduce the discrepancy (Keek et al. 2009). Alternatively, it may be the result of a higher local accretion rate.

The transition of the thermonuclear burning behavior in the atmosphere after a superburst is solely due to the temperature change, whereas the mass accretion rate remains constant. Note that in practice the mass accretion rate can vary on the time scale of a superburst, which would provide an effect additional to the change in the burning behavior. Because the cooling after a superburst sets the thermal profile of the envelope, this poses strict constraints on the environment in which the first bursts ignite. Detecting the transition of stable to unstable burning after a superburst will allow us to determine the column depth and temperature at which the transition occurs. These are important ingredients for improving the current models. Unfortunately, the observations of bursts after a superburst are scarce, and at the moment of writing the actual transition has not been observed.

In this paper we provide one-dimensional multi-zone

models of a neutron star envelope that undergoes a superburst. We create models with, respectively, a carbon-rich, a helium-rich, and a solar-composition atmosphere. We self-consistently simulate both the superburst and the burning processes in the atmosphere. The burst quenching is followed, as well as the transition to unstable burning and the return of bursts. We focus on the nuclear reactions that are responsible for the different phenomena in the light curves. Finally, we combine a large set of observations to place constraints on burst quenching.

2. NUMERICAL METHOD AND OBSERVATIONS

The one-dimensional models of the neutron star envelope presented in this paper are similar to the superburst models by Keek & Heger (2011). We refer to that study for a detailed description of the code employed and the setup of the models. Here we describe the main properties of our simulations, as well as the differences with respect to the models by Keek & Heger (2011). Most notable are the use of a different prescription for electron conductivity and a different implementation of accretion, which may cause small differences in the ignition conditions of superbursts.

2.1. *Stellar Evolution Code*

We create and evolve one-dimensional models of the neutron star envelope using the implicit hydrodynamics stellar evolution code KEPLER (Weaver et al. 1978). The version of KEPLER that we use is similar to the version used in recent studies (e.g., Woosley et al. 2002, 2004; Heger et al. 2007a). We employ an adaptive one-dimensional Lagrangian grid in the radial direction, under the assumption of spherical symmetry. To follow the chemical evolution we use a large adaptive nuclear network (Rauscher et al. 2003) including the hot-CNO cycle (Wallace & Woosley 1981), the 3α -, rp -, and ap -processes, carbon fusion, and photodisintegration. We take into account neutrino energy loss (Itoh et al. 1996), as well as radiative opacity and electron conductivity (Iben 1975). Mixing of the chemical composition by convection, semiconvection, and thermohaline circulation is implemented as a diffusive process using mixing-length theory (e.g., Clayton 1968).

Mass accretion is implemented by increasing the pressure of the outermost zone in the model at each time step (see also Woosley & Weaver 1984; Taam et al. 1996). Periodically a zone is added on top. Because of the details of the implementation, this causes a small dip in the light curve. We carefully check that this does not influence any of the conclusions that we draw about the bursting behavior. The light curves in this paper are corrected by omitting the brief time intervals when the dips occur.

2.2. *Model Setup*

We model the neutron star envelope above a radius of 10 km and an enclosed mass of $1.4 M_{\odot}$, up to the surface. The bottom of the surface zone is at a column depth of $y = 10^6 \text{ g cm}^{-2}$. This is well below the typical column depth for hydrogen/helium bursts of $y \simeq 10^8 \text{ g cm}^{-2}$. The inner part of the model is formed by a $2 \times 10^{27} \text{ g}$ iron substrate. It serves as a buffer into which heat generated by the superburst can flow, and diffuse outward

on longer time scales. This ensures a correct late-time light curve.

Crustal heating is taken into account by a constant luminosity at the inner boundary equivalent to $Q_b = 0.2 \text{ MeV nucleon}^{-1}$. Because of neutrino cooling in the substrate, the effective amount of crustal heating at the top of the substrate, close to the superburst ignition depth, is $Q_b = 0.1 \text{ MeV nucleon}^{-1}$. This is in the range of typically assumed values for superbursters at accretion rates above 10% of the Eddington limit (e.g., Haensel & Zdunik 1990; Cumming et al. 2006).

On top of the substrate we accrete a mixture of 80% ^{56}Fe and 20% ^{12}C . The latter is the typical mass fraction of carbon that Cumming et al. (2006) found from fits to observed light curves of hydrogen accreting superbursters, and ^{56}Fe is the most abundant isotope in the ashes of hydrogen-rich bursts (e.g., Woosley et al. 2004). The ashes of helium-rich bursts consist mostly of somewhat lighter isotopes: ^{28}Si , ^{32}S , ^{36}Ar , ^{40}Ca (e.g., Joss & Li 1980). For our models, however, we use ^{56}Fe , in order to have a consistent opacity of all envelope models, giving comparable ignition conditions for the superburst.

Accretion of a hydrogen or helium-rich atmosphere is done only briefly before the superburst, because the computational expense of simulating the many short bursts that occur before the superburst is prohibitive. From a model where only a carbon-rich mixture was accreted we know already the moment of superburst ignition. 12.7 hr before this time, we replace the accretion composition by a solar (71% by mass ^1H , 27% ^4He , 2% ^{14}N), or a helium-rich mixture (98% ^4He , 2% ^{14}N). This allows for several hydrogen and/or helium bursts to take place before the superburst, ensuring equilibrium is reached for the effects of chemical inertia (Woosley et al. 2004). The change of accretion composition does not affect the ignition of the superburst, because it depends on the pressure at the bottom of the carbon layer, which continues to increase at the same rate. Moreover, at that time the initial phase of the carbon runaway has already started.

An accretion rate of $\dot{M} = 5.25 \times 10^{-9} M_\odot \text{ yr}^{-1}$ is used. For an atmosphere of solar composition on a neutron star of $1.4 M_\odot$ this corresponds to 30% of the Eddington-limited rate $\dot{M}_{\text{Edd}} = 1.75 \times 10^{-8} M_\odot \text{ yr}^{-1}$.

The presented results are not corrected for the redshift due to the neutron star's gravity (see also Keek & Heger 2011). Our Newtonian model has the same surface gravity as when general relativity is taken into account for a star with the same mass and a 11.2 km radius, which has a gravitational redshift of $z = 0.26$ (e.g., Woosley et al. 2004).

Based on the atmosphere composition, we refer to the simulations as model ‘‘C’’, ‘‘He’’, and ‘‘H’’ (Table 1).

2.3. MINBAR Catalog of Observations

To derive observational constraints on the bursting behavior of superbursters we employ version 0.51 of the Multi-INstrument Burst ARchive (MINBAR; Keek et al. 2010; see <http://users.monash.edu.au/~dgallo/minbar> for more details). This catalog contains the results of the analysis of 4,192 observed Type I X-ray bursts from 72 sources as well as 27,340 pointings on 84 sources. The observations have been performed with the Wide-Field

Cameras (WFCs) on board the *Beppo Satellite per Astronomia X* (*BeppoSAX*; Cornelisse et al. 2003) and the Proportional Counter Array (PCA) on board the *Rossi X-Ray Timing Explorer* (*RXTE*; Galloway et al. 2008). Both instruments are sensitive in a similar energy range above 2 keV. Because of its larger collecting area, the PCA is more sensitive to faint bursts (e.g., Keek et al. 2010).

MINBAR comprises the largest collection of X-ray bursts available, but we refer to the literature if more constraining observations have been reported.

3. RESULTS

3.1. Hydrogen/Helium Atmosphere Models

Initially the accretion of carbon-rich material is simulated to self-consistently build up a neutron star envelope close to the ignition of a superburst. Approximately half a day before the thermonuclear runaway of carbon burning sets in, the accretion composition is changed. We create three different models: one accreting solar composition (model H), one with helium-rich material (model He), and for comparison one where we retain the carbon-rich atmosphere (model C). From that moment we follow both the carbon burning in the ocean and the hydrogen/helium burning in the atmosphere. Several normal X-ray bursts occur before the superburst (Fig. 1, 2). During the superburst decay, hydrogen and helium burn stably: bursts are quenched. Once the envelope has cooled sufficiently, unstable burning resumes. At the transition, oscillatory burning takes place (marginally stable burning). The first bursts after the superburst are less energetic and have shorter recurrence times than the bursts before the superburst. When the envelope cools down further, the recurrence times become longer and the bursts become as energetic as they were before the superburst. For the models H and He we calculate over 900 bursts per model.

3.2. Superburst

The superburst occurs 1.28 years after the start of the simulations, after accreting a column of $y = 1.1 \times 10^{12} \text{ g cm}^{-2}$. Its ignition is not in-phase with the occurrence of hydrogen/helium bursts (Fig. 1, 2): flashes in the envelope do not trigger the runaway carbon burning. The superburst occurs slightly earlier in the models H and He compared to C: 1.1 minutes for helium accretion and 5.2 minutes for solar composition. This may be due to heating from hydrogen and helium burning, but the differences in recurrence time, and therefore ignition depth, are too small to cause substantial differences in, for example, the superburst fluence or other observables. The amount of time before the superburst during which we simulate the hydrogen/helium bursts may not have been long enough to bring the model into thermal equilibrium, and the deeper layers could still be increasing somewhat in temperature because of heating by the bursts. Because most of the energy produced by the bursts is radiated away from the surface, however, this introduces only a minor deviation in the temperature at the carbon ignition depth, which can be modeled by a slightly higher effective Q_b .

The superbursts start with a detonation, which drives a shock toward the surface, and produces a brief shock

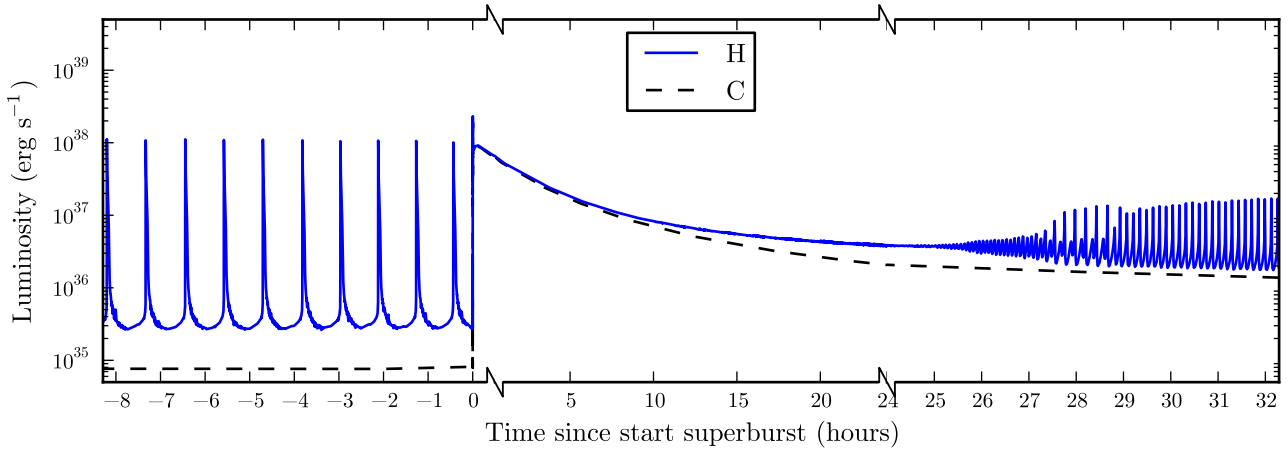


FIG. 1.— Light curve of models H and C. Breaks on the axis indicate a change in time scale. Only a small fraction of the simulated bursts after the superburst are shown.

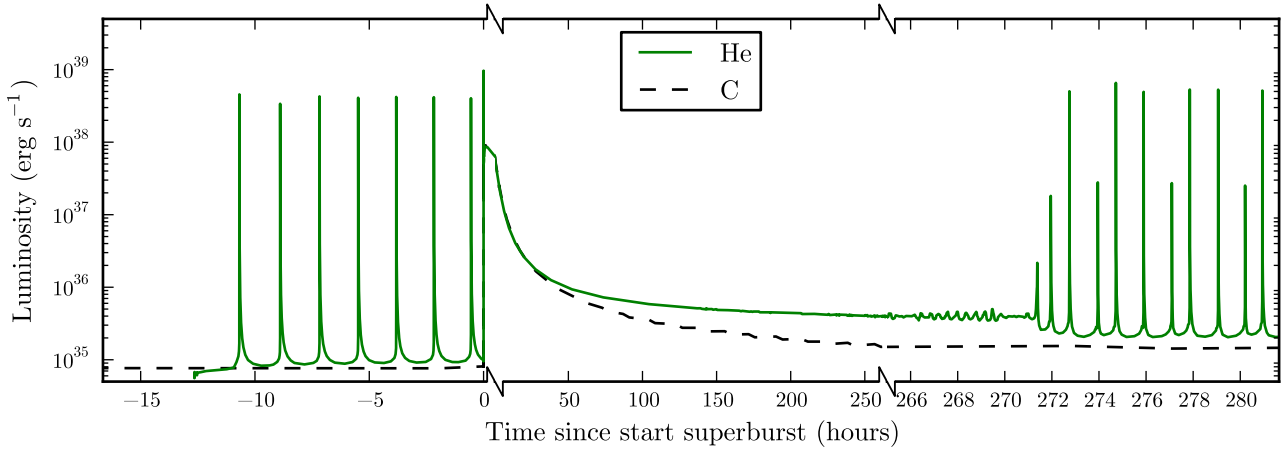


FIG. 2.— Light curve of models He and C. Breaks on the axis indicate a change in time scale. Only a small fraction of the simulated bursts after the superburst are shown.

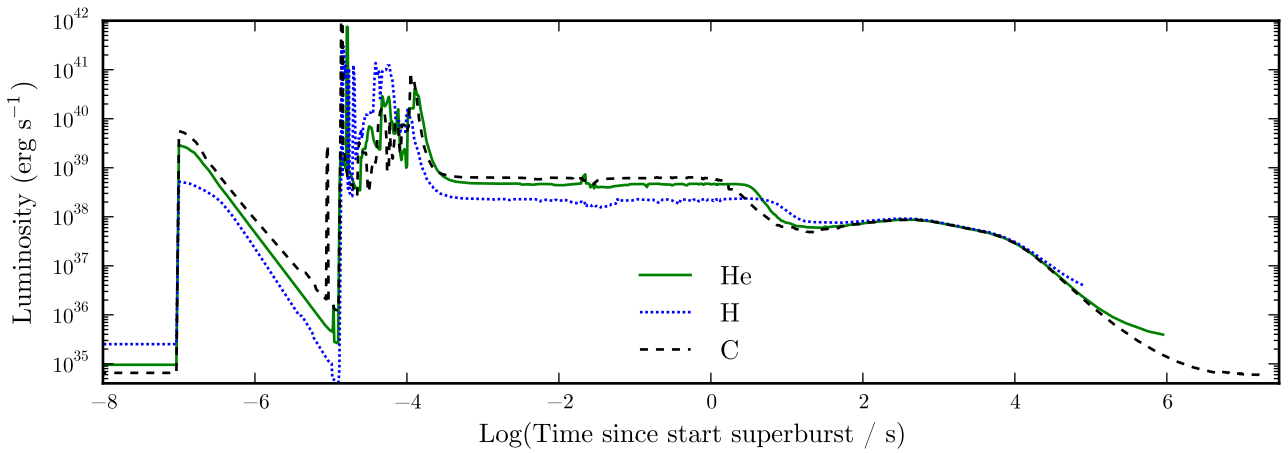


FIG. 3.— Logarithmic light curve of superbursts from models He, H, and C. The curves end when the burst-quenching period ends, or, in the case of a carbon-rich atmosphere, when the next superburst occurs.

TABLE 1

PROPERTIES OF SUPERBURSTS AND SUBSEQUENT BURSTS FOR DIFFERENT ATMOSPHERE COMPOSITIONS

Model	C	He	H
Accretion composition (mass fractions)	0.2 ^{12}C 0.8 ^{56}Fe	0.98 ^4He 0.02 ^{14}N	0.71 ^1H 0.27 ^4He 0.02 ^{14}N
L_{peak} (10^{37} erg s $^{-1}$)	8.7	8.8	9.3
$E_{\text{shock br}}$ (10^{32} erg)	7.7	4.4	1.4
$L_{\text{shock br}}$ (10^{39} erg s $^{-1}$)	10	6.2	1.3
Precursor duration (s)	1.2	3.2	5.7
$E_{\text{precursor}}$ (10^{39} erg)	0.75	1.5	1.3
t_{minimum} (s) ^a	20	25	42
t_{quench} (days)		11.3	1.1
P_{osc} (minutes) ^b		20	5.0
t_{return} (days) ^c		115	35

^a Time of minimum luminosity between precursor and peak.

^b Period of oscillatory burning.

^c Time when burst properties return to pre-superburst values.

breakout peak in the light curve (Fig. 3), followed on a dynamical time-scale by a precursor burst. The superburst peak is reached 6.4 minutes after the superburst onset. Stable hydrogen (helium) burning produces a peak luminosity, L_{peak} , that is 5% (0.4%) higher for model H (He) compared to C (Table 1). The decays follow the same two-component power-law profile, with again hydrogen burning raising the luminosity by a few percent. The light curves for the models H and C deviate from the cooling curve of C when the luminosity becomes comparable to that from stable hydrogen or helium burning. The hydrogen or helium burning contribution to the total luminosity exceeds 10% after roughly $\sim 2 \times 10^4$ s for model H, and after $\sim 1 \times 10^5$ s for He. For all models a small amount of carbon burns at the bottom of the newly accreted material. The burning time scale, however, is much longer than the accretion time, so this is not steady-state burning, but leads up to the next superburst.

3.3. Shock Breakout

After the superburst detonation, a shock travels outward from the bottom of the carbon-rich layer. Once it reaches the surface, a shock breakout peak is produced in the light curve (Fig. 3). We determine its maximum luminosity, $L_{\text{shock br}}$, and its fluence, $E_{\text{shock br}}$, as measured within 5×10^{-6} s after the onset (Table 1). The differences in $L_{\text{shock br}}$ trace variations in the opacity of the outer atmosphere.

The shock accelerates the outer zones, where the density is lowest, and the shock over-pressure is highest, to a substantial fraction of the speed of light within a very short time interval. This behavior is likely not well resolved by our model, and at times introduces large variability in, for example, the luminosity in the outer zones during the shock breakout and the start of the subsequent precursor burst. During this part of the superburst we take the mean luminosity of the 10 outermost zones to reduce the effect on the light curve, although some of the introduced variability remains visible (Fig. 3).

3.4. Precursor

Most of the energy of the shock is used to expand the outer layers. They fall back on a dynamical time scale of 10^{-5} s, and dissipate that energy into heat, which powers a precursor burst that reaches the Eddington limit.

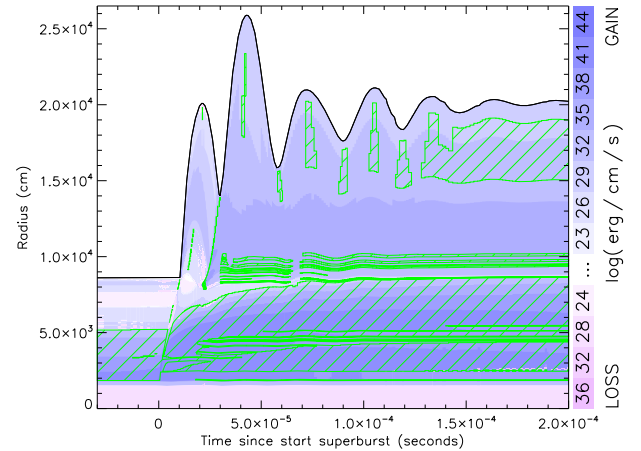


FIG. 4.— For model He: energy generation/loss (color scale) in the neutron star envelope as a function of time in a short interval around the superburst onset. Green hatching indicates convection (Rayleigh–Taylor instabilities).

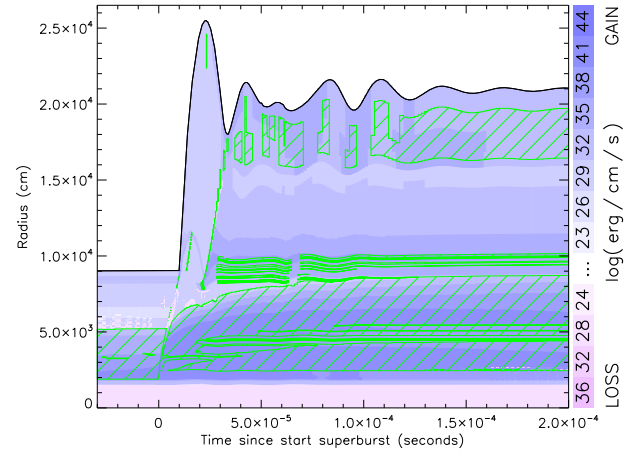


FIG. 5.— Same as Fig. 4 for model H.

At the start of the precursor burst, the fallback causes the material to settle while undergoing a damped oscillation. This creates corresponding variability of super-Eddington luminosity as high as 3.7×10^{40} erg s $^{-1}$ (Fig. 4, 5).

The precursor light curves are dependent on the atmospheric composition (Fig. 3). The heating of the atmosphere instigates the burning of hydrogen and/or helium upon fallback (Fig. 4, 5), leading to a thermonuclear runaway. This adds to the precursor fluence $E_{\text{precursor}}$ (Table 1). In model H 26% of the 7.4×10^7 g column of solar composition is burned, and in model He 67% of the 9.0×10^7 g helium column. Because of the difference in energy yield of the hydrogen and helium burning nuclear reactions, the total energy released and, hence, the fluence is very close for these particular compositions.

The luminosity reaches a plateau caused by photospheric radius expansion (PRE, Fig. 3). We compute the duration of the PRE phase as the time from the precursor onset to the time when the luminosity drops below 90% of the plateau value (Table 1).

After the PRE phase, the luminosity drops quickly, reaching a minimum at t_{minimum} (Table 1), and sub-

sequently climbing to the superburst peak at approximately 400 s.

The precursor light curve contains some irregularities. In the figures we have filtered out strong variations occurring from one time step to the next, that are due to the outer few grid points, and not representative of the overall behavior of the model.

3.5. Bursts in a Helium-rich Atmosphere

First we discuss the effect of the superburst on the thermonuclear processes in model He. After the superburst precursor, helium burning in the atmosphere proceeds in a stable manner. Bursts only reappear once the envelope has cooled down sufficiently after 11.3 days (Fig. 2).

Before bursts resume, the burning is marginally stable when the temperature in the atmosphere drops to 3×10^8 K, leading to oscillations in the light curve with a period close to 20 minutes (Fig. 6). The oscillations have a small amplitude of at most approximately 10% of the average luminosity, and numerical noise dampens the oscillations during certain periods. Once the bursts start, the burst peak flux increases, and the third burst already has a peak luminosity comparable to the bursts before the superburst (Fig. 6, 7). During 2.3 days we find both bright bursts with a peak luminosity of $L_{\text{peak}} \simeq 4 \times 10^{38} \text{ erg s}^{-1}$ (the Eddington luminosity for a hydrogen-deficient atmosphere) and weaker bursts with $L_{\text{peak}} \simeq 3 \times 10^{37} \text{ erg s}^{-1}$. The bright as well as the weak bursts have a relatively slow rise of the light curve. During this time 3α is the predominant nuclear process, producing ^{12}C . In the bright bursts 3α raises the temperature sufficiently for α -captures to take over, causing a faster rise of the luminosity, and producing mostly ^{28}Si . The bright bursts heat the envelope sufficiently for additional stable helium burning to take place, followed by a weak burst. Stable helium burning reduces the helium content of the atmosphere, leading to a burst with a lower L_{peak} . The weak burst does not heat the envelope enough for additional stable burning, such that the next burst is again bright, and ignites after a shorter recurrence time. While the envelope continues to cool from the superburst, the number of bright bursts in between weak bursts increases, until after 2.3 days the weak bursts disappear.

Comparing the profiles of individual bursts after the quenching period, the weak bursts have a relatively long rise of ~ 5 s (Fig. 8). The early bright bursts share this slow rise to a similar luminosity as the peak of the weak bursts, but then transition in a fast sub-second rise to the Eddington luminosity. Later bright bursts show an initial ‘‘bump’’ that decreases in duration over time. The bursts from before the superburst show a slow rise component with a duration of 0.4 s. The decay of the bursts becomes longer as the recurrence time increases, reflecting the longer thermal time scales of increasing ignition depths.

The flux from the accretion process at a rate of $\dot{M} = 5.25 \times 10^{-9} M_{\odot} \text{ yr}^{-1}$ for a neutron star of $1.4 M_{\odot}$ with a 10 km radius is $4.35 \times 10^{37} \text{ erg s}^{-1}$ (assuming isotropic emission and a 100% efficient accretion process). The initial oscillations and weak bursts have a lower L_{peak} , but the brighter bursts outshine the accretion flux by approximately a factor 10.

The superburst burns most carbon out to $y \simeq 7 \times 10^8 \text{ g cm}^{-2}$. Between this depth and the ignition depth of the helium bursts at $y \simeq 1 \times 10^8 \text{ g cm}^{-2}$, a carbon mass fraction of 0.1 survives the runaway burning, but burns on a longer time scale. Carbon burns through $^{12}\text{C}(^{12}\text{C}, \alpha)^{20}\text{Ne}$ and subsequent α -capture reactions, producing predominantly ^{28}Si . When we stop the simulation, the carbon mass fraction of this material varies from 2×10^{-3} down to 2×10^{-4} .

Directly after the superburst, during the burst quenching period, helium burns stably to carbon by the 3α -process. Captures of α on ^{12}C and ^{14}N from the accretion composition produce a limited fraction of ^{16}O , ^{18}F , and heavier isotopes up to magnesium (Fig. 9). Over time, as the atmosphere cools down, the α -capture rates reduce, and only lighter elements up to neon are produced. The main product of nuclear burning during the quenching period, however, is ^{12}C , with a mass fraction of 95%. After the quenching period, this material is compressed to higher densities, and $^{12}\text{C}(^{12}\text{C}, \alpha)^{20}\text{Ne}$ reduces the carbon mass fraction. Subsequent α -capture reactions produce mainly ^{28}Si , ^{32}S , and ^{36}Ar . The next superburst ignition occurs close to the bottom of this layer, and depends on the remaining carbon fraction. When we end the simulation, the ^{12}C fraction is 23%, and still dropping.

During the quenching period, most burning takes place close to $y \simeq 10^8 \text{ g cm}^{-2}$, but not all helium is burned. Some survives down to a depth of $y \simeq 10^{10} \text{ g cm}^{-2}$. The low mass fraction ($Y \lesssim 10^{-3}$) makes 3α inefficient, but series of α -captures ($^{12}\text{C}(\alpha, \gamma)^{16}\text{O}(\alpha, \gamma)^{20}\text{Ne}(\alpha, \gamma)^{24}\text{Mg}$) still occur. After stable burning at $y \simeq 10^8 \text{ g cm}^{-2}$ ends, the α -captures in the deeper layers continue until helium is fully depleted. During this time, even though the helium mass fraction is low, because of the large total mass down to $y \simeq 10^{10} \text{ g cm}^{-2}$, the captures contribute a substantial fraction of the total generated energy at any given time. This effectively slows down the cooling for up to 8.1 days, keeping the recurrence time of the bursts constant. Once helium is depleted at these depths, the cooling continues, and the burst recurrence time increases over time. 46.3 days after burst resumption the recurrence time is 88 minutes, whereas the pre-superburst recurrence time was 100 minutes. We stop the simulation here, but extrapolating the trend, the original recurrence time will be recovered approximately 115 days after burst resumption.

The model produces bursts with a spread of $\sim 50\%$ in L_{peak} (Fig. 7) with a quasi-periodic behavior. To a lesser extent these variations can also be seen in t_{recur} . This is caused by the dependence of the ignition conditions of a burst on the previous bursts, based on, e.g., the fraction of helium that was burned, the heat deposition, and compositional inertia.

3.6. Bursts in a Solar-composition Atmosphere

Burst quenching is also present in model H (Fig. 1, 10). Directly following the superburst, hydrogen and helium burning is stable. Helium burns by the 3α -process, providing CNO elements which facilitate hydrogen burning by the hot-CNO cycle. Break-out from this cycle by $^{15}\text{O}(\alpha, \gamma)^{19}\text{Ne}$ allows for a rapid series of proton captures and β -decays (rp -process) to produce mostly ^{66}Ga and ^{66}Ge , whereas a large number of isotopes with mass

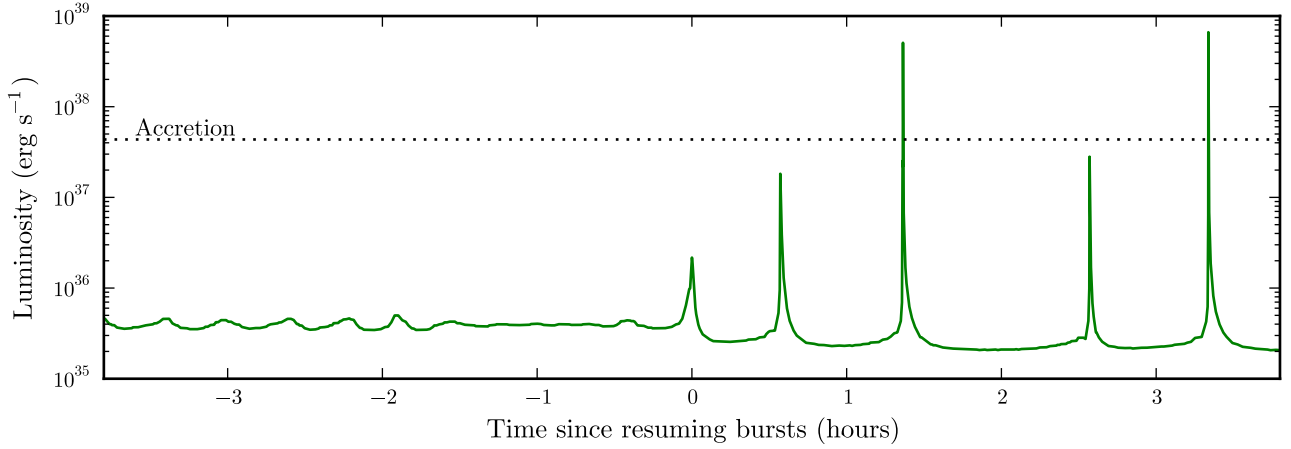


FIG. 6.— Light curve of model He at the time when quenching stops and bursting resumes. The dotted line indicates the level of the accretion flux.

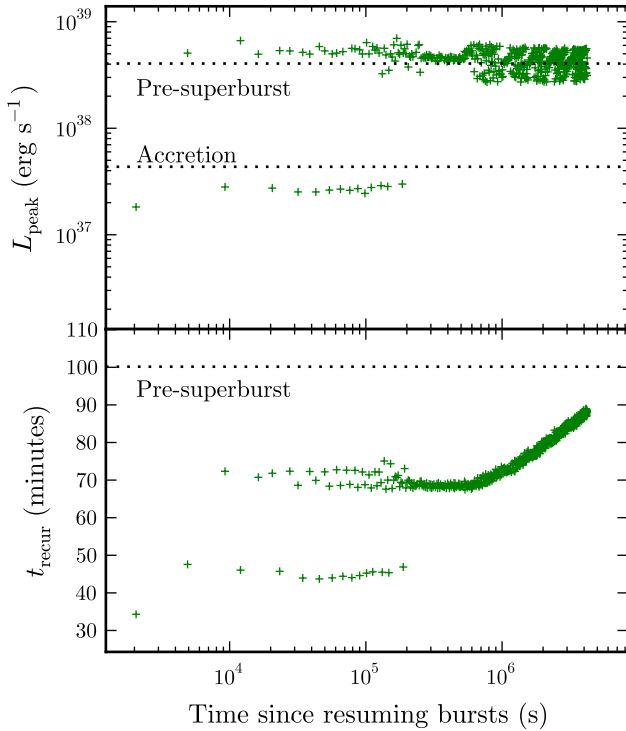


FIG. 7.— Peak luminosity L_{peak} and recurrence time t_{recur} of bursts after the quenching period for model He. The dotted lines indicate the mean values for bursts before the superburst and the luminosity of the accretion process.

numbers in the range of 59–72 contribute mass fractions of several percents (Fig. 11).

Similarly to model He, after the superburst a layer with a ^{12}C mass fraction of 10% remains between $y \simeq 1 \times 10^8 \text{ g cm}^{-2}$ and $y \simeq 7 \times 10^8 \text{ g cm}^{-2}$. It burns on a longer time scale down to a mass fraction of 2×10^{-4} . Hydrogen and helium burning during the burst quenching period produce carbon at a mass fraction of 5%. Nuclear burning on longer time scales reduces the carbon mass fraction in this layer to 10^{-3} .

Burst quenching is much shorter than in the model with a helium-rich atmosphere: bursts resume after 1.1 days. As the superburst cools, the temperature

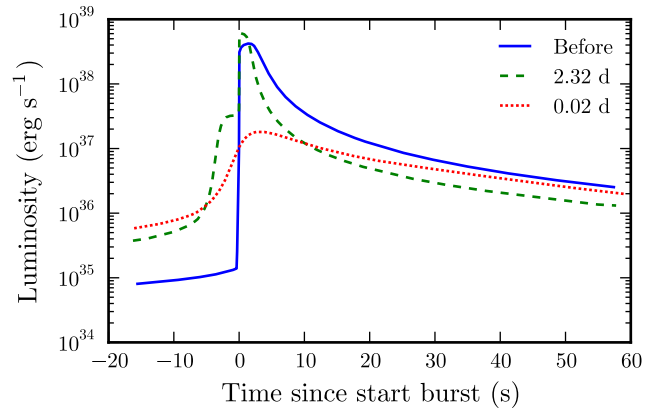


FIG. 8.— Comparison of light curves of helium bursts aligned on the peak. The smallest burst occurred 34 minutes after bursts resumed, and the one with the bump before the peak occurred after 2.3 days. The burst with the longest decay occurred before the superburst. Superburst emission has been subtracted for all bursts.

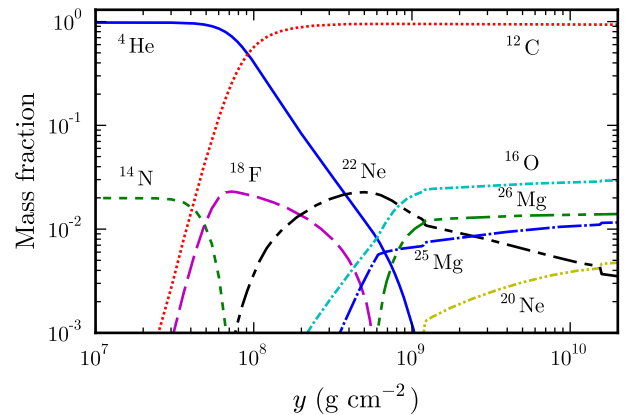


FIG. 9.— Composition of the envelope at the end of the burst quenching period, down to the bottom of the layer of ashes from stable helium burning. Only the most abundant isotopes are shown.

drops below $4.3 \times 10^8 \text{ K}$, and the breakout reaction $^{15}\text{O}(\alpha, \gamma)^{19}\text{Ne}$ becomes less efficient than the 3α -process. Whereas at higher temperatures the break-out reactions

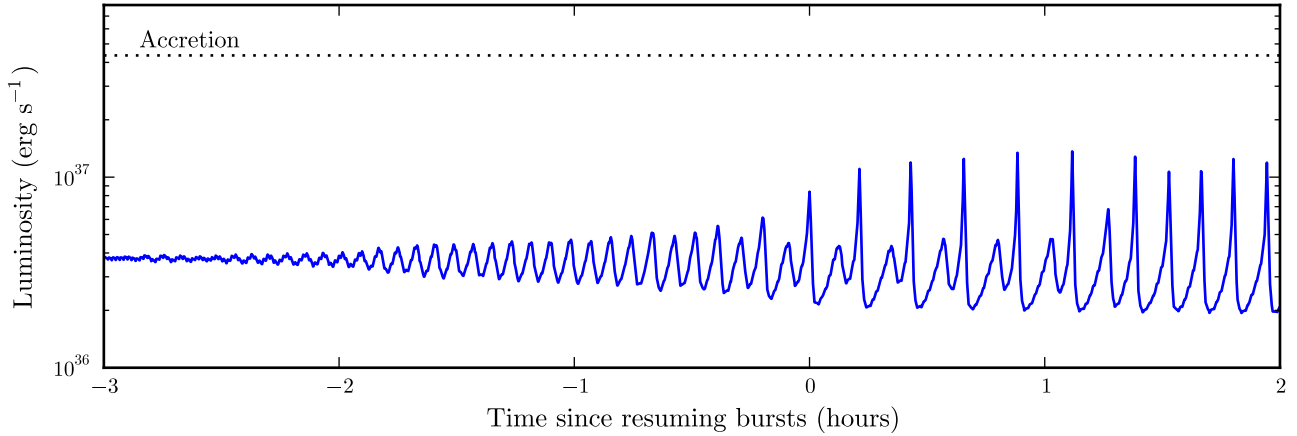


FIG. 10.— Light curve of model H at the time when quenching stops and bursting resumes. The dotted line indicates the level of the accretion flux.

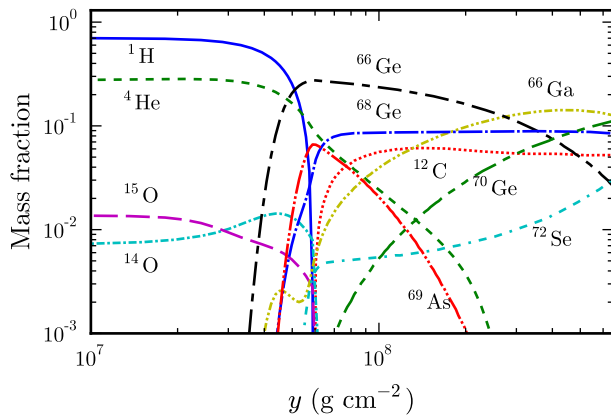


FIG. 11.— Composition of the envelope at the end of the burst-quenching period, down to the bottom of the layer of ashes from stable burning of solar-composition material. Only a selection of the most abundant isotopes is shown.

quickly removed CNO elements, now the CNO mass fraction is growing. This causes an increase in the helium production through the CNO cycle, and results in the increase of the energy generation rate of both the CNO cycle and the 3α -process. The involved reactions raise the atmosphere temperature until once more the $^{15}\text{O}(\alpha, \gamma)^{19}\text{Ne}$ break-out can efficiently remove most of the CNO elements, providing seed nuclei for the rp -process, which captures most of the hydrogen. With hydrogen and the CNO isotopes gone, the CNO cycle and rp -process switch off, reducing the helium production, and thereby the 3α rate, allowing the atmosphere to cool down. Note that while hydrogen is depleted, helium is not. As fresh hydrogen and helium are accreted and mixed in from layers closer to the surface, the cycle repeats itself. This produces a series of oscillations in the light curve, that announces the end of the steady-state burning of the burst quenching phase (Fig. 10). The time scale for the oscillations is 5.0 min.

The oscillations increase in amplitude over time. After 2.1 hr the $^{15}\text{O}(\alpha, \gamma)^{19}\text{Ne}$ breakout and subsequent rp -process increase the temperature during the oscillations sufficiently for the $^{14}\text{O}(\alpha, p)^{17}\text{F}(p, \gamma)^{18}\text{Ne}$ breakout reactions initiate the αp -process, which causes a faster rise of the luminosity, producing small bursts instead of os-

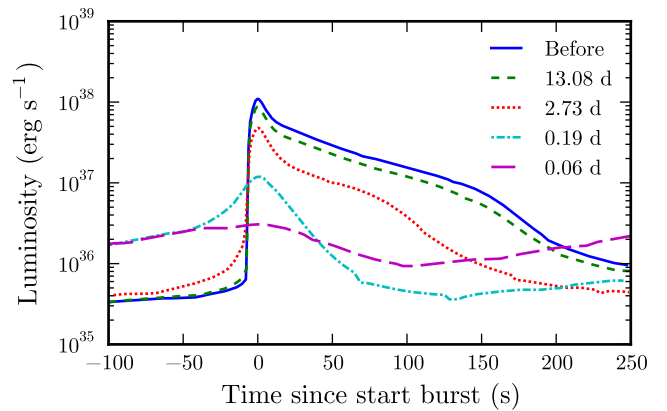


FIG. 12.— Comparison of light curves of hydrogen/helium bursts aligned on the peak. From small peak to high, the bursts occurred 1.5 hr, 4.6 hr, 2.7 days, and 13.1 days after bursting resumed, respectively. The brightest burst occurred before the superburst. Superburst luminosity has been subtracted for all bursts.

cillations. For ~ 1.5 hr oscillations and small bursts alternate, until an equilibrium is reached and only small bursts occur (Fig. 10). The bursts following an oscillation have a shorter recurrence time. Initially the bursts have a slow rise, similar to the oscillations, and a faster decay. Over time, the rise shortens, and the decay lengthens (Fig. 12).

When the oscillations have disappeared, and only bursts remain, the recurrence time is constant at 8.2 minutes until approximately 1.2 days after burst resumption. As in model He, this is due to the burning of residual helium at greater depths, which delays the cooling of the atmosphere. Although the recurrence time is constant, the peak luminosity L_{peak} increases with time.

Afterward both the recurrence time and L_{peak} increase with time (Fig. 13). After 13 days $t_{\text{recur}} = 39$ minutes is reached. The burst peak luminosity is then at 77% of the pre-superburst level. The burst light curve approaches the profiles of the bursts before the superburst. At this time we end the simulation. Extrapolating, the recurrence time of 52 minutes of the bursts before the superburst will be reached approximately 35 days after burst resumption.

For $1 \times 10^5 \lesssim t \lesssim 4 \times 10^5$ s there are some ‘oscilla-

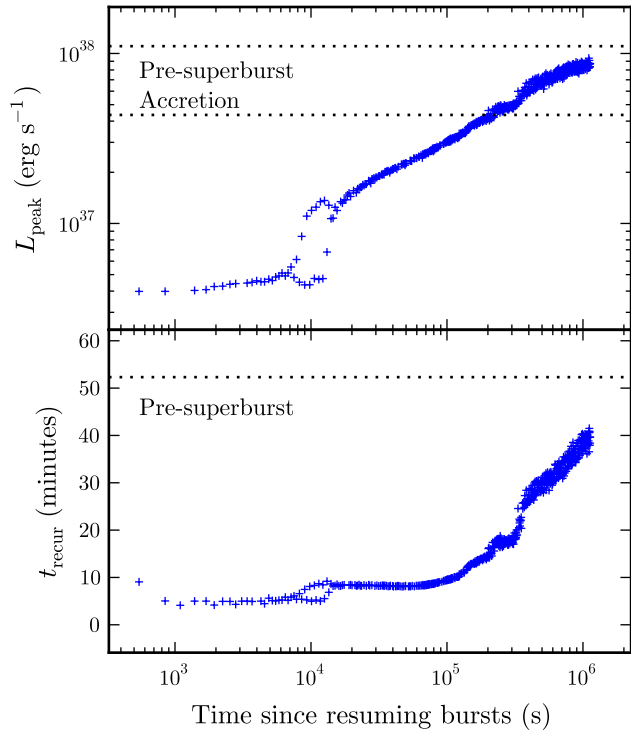


FIG. 13.— Peak luminosity L_{peak} and recurrence time t_{recur} of bursts after the quenching period for model H. The dotted lines indicate the mean values for bursts before the superburst and the luminosity of the accretion process.

tory’ variations in both t_{recur} and L_{peak} , which are likely of similar origin as the late-time variations in the burst properties in the helium-rich atmosphere (Fig. 13).

3.7. Observational Limits on Burst Quenching

The first normal burst observed from a source after a superburst provides an upper limit to the burst quenching time. For all known (candidate) superbursts, we identify the first detected burst either from MINBAR, or from the literature (Table 2). The superbursts from 4U 1735–444 and 4U 1820–303 occurred when (or close to when) the source exhibited a persistent flux where no or very few bursts have been detected for the respective sources. Most probably hydrogen and helium were undergoing steady-state burning already before the superburst started. For this reason we exclude these superbursts when we investigate constraints on burst quenching. Furthermore, we do not consider the recent superbursts from EXO 1745–248, SAX J1747.0–2853, and SAX J1828.5–1037, which are still being analyzed at the moment of writing, nor those from GX 17+2, which has an atypically high mass accretion rate (in ’t Zand et al. 2004).

Two superbursters are so-called ultracompact X-ray binaries (UCXBs; e.g., in ’t Zand et al. 2007), where the accreted material is thought to be hydrogen deficient, but may contain helium: 4U 0614+091 (Kuulkers et al. 2010) and 4U 1820–303 (Strohmayer & Brown 2002; in ’t Zand et al. 2011; see also Cumming 2003). From 4U 0614+091 two bursts were observed in the period after the superburst: after 18.6 and 34.9 days, respectively (Kuulkers et al. 2010). Both bursts reach a bolometric peak flux that is consistent within 1σ . The first burst is

TABLE 2
OBSERVATIONAL LIMITS ON BURST QUENCHING FOR ALL KNOWN (CANDIDATE) SUPERBURSTS

Source	Time (MJD) ^a	First burst (d) ^b	t_{exp} (hr) ^c
4U 0614+091	53441.70 (-0.26)	18.6 ^d	0.9
4U 1254–690	51187.39	124.7	25.5
4U 1608–522 ^t	53495.08	99.8 ^e	2.6
4U 1636–536	50253.61 (-0.07)	96.3	0.0
	50642.37 (-0.07)	68.6	2.1
	51324.21 (-0.06)	15.0	33.9
	51962.70	22.8	9.7
KS 1731–260	50349.42	34.4	48.0
4U 1735–444	50318.13 (-0.02)	374.3 [*]	130.6
EXO 1745–248 ^t	55858.53 (-0.06)	-	-
GX 3+1	50973.04 (-0.08)	94.2	2.5
SAX J1747.0–2853 ^t	55605.54	25.1 ^f	-
GX 17+2	50340.30 (-0.03)	2.2	36.6
	51444.10 (-0.04)	- ^g	132.0
	51452.33	2.3	113.4
	51795.34	12.8	100.5
4U 1820–303	51430.07	167.0	113.7
	55272.72 (-0.06)	- [*]	-
SAX J1828.5–1037 ^t	55877.34 (-0.06)	-	-
Ser X–1	50507.08 (-0.03)	34.6	45.9
	51399.14 (-0.07)	309.4	1.5
	54753.28 (-0.07)	54.7	0.0

^a Time of the observed start of the superburst (see Sect. 1 for references). In case this directly follows a data gap, the duration of the gap is indicated in parenthesis.

^b Using bursts from MINBAR, unless indicated otherwise.

^c Total exposure time in first 35 d after the superburst; “-” indicates the superburst occurred outside of the period covered by the catalog.

^d Kuulkers et al. (2010).

^e Keek et al. (2008).

^f Linares et al. (2011a).

^g There were no bursts observed before the subsequent superburst.

^{*} Superburst took place when hydrogen and helium were likely burning in steady state.

^t Transient source with outburst durations shorter than the superburst recurrence time.

more symmetric with a rise of 5 s and a decay of 2.0 s, whereas the second one has a faster rise of 1 s and a slower decay of 13.0 s. It should be noted, however, that the rise and decay time scales were derived from different energy bands, with the first burst being observed at higher energies, causing part of the shorter decay time.

The other superbursting sources are thought to accrete hydrogen-rich material. As the model with the hydrogen-rich envelope predicts normal bursting behavior to return in 35 days, we identify the bursts from MINBAR observed in that period, as well as the net exposure time, t_{exp} , of all observations, including those without bursts (Fig. 14, Table 2). The earliest observed normal burst occurred 15.0 days after the superburst from 4U 1636–536 on MJD 51324.21. After most superbursts the total exposure time is short, and observations are infrequent. Therefore, we combine the data for these sources in 1 day time bins to be able to distinguish changes in the burst behavior on similar time scales as exhibited by our models. To place constraints on the burst recurrence time, t_{recur} , we use the combined t_{exp} and number of bursts during each day, taking into account the presence of data gaps by Earth occultations and by passages through the South Atlantic Anomaly.

Data gaps reduce the fraction of the observation time t_{obs} when bursts can be observed: $t_{\text{exp}} = \eta t_{\text{obs}}$, with η the observation efficiency. For $\eta < 1$ bursts can be missed,

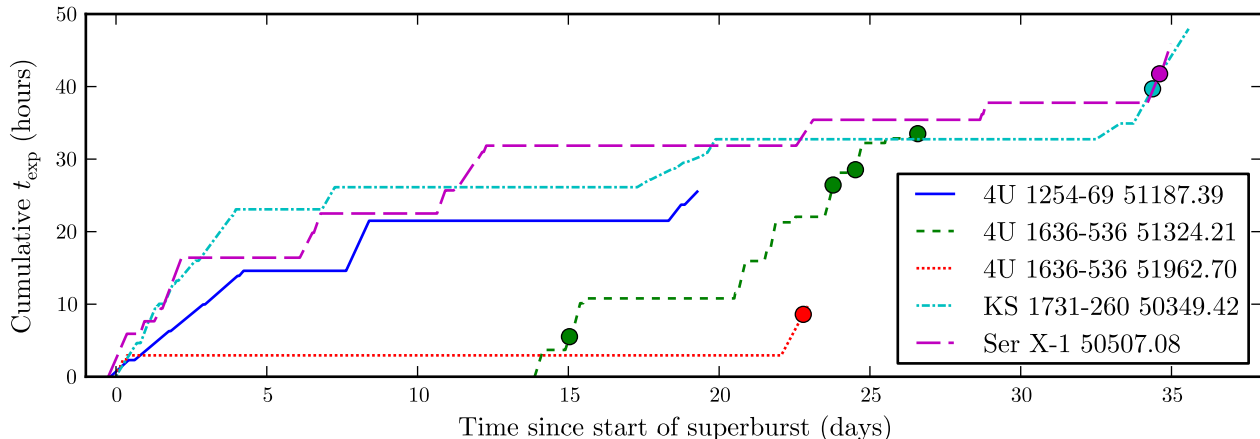


FIG. 14.— Cumulative net exposure time during 35 days after a superburst for hydrogen-accreting sources. We exclude sources with less than 3 hr of exposure time, and those for which hydrogen/helium burning is stable, as well as GX 17+2 (see also Table 2). For each superburst we indicate the source name and the time of the superburst (MJD). Circles indicate the detection of normal bursts.

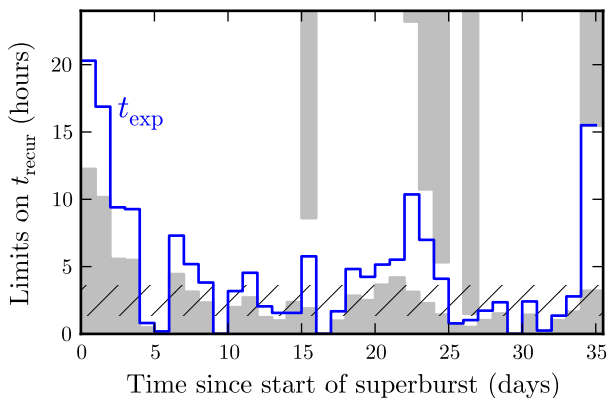


FIG. 15.— Observational limits on the burst recurrence time t_{recur} from combined observations after the superbursts from Fig. 14 in 1 day time bins. The region between the gray areas is the 90% confidence region for t_{recur} . The solid line is the net exposure time t_{exp} per day, and the hatched region indicates the range of minimum values of t_{recur} observed for bursts at similar persistent flux as at the time of the superbursts.

and when N bursts occur, $n \leq N$ are detected. Using a binomial distribution, the probability P of detecting n bursts out of N is

$$P(n; N, \eta) = \binom{N}{n} \eta^n (1 - \eta)^{N-n}.$$

Since n and η are known for each observation, we use P to identify those values of N for which the probability of detecting n is largest. After normalization, we determine the 90% confidence region for N , which we use to constrain $t_{\text{recur}} = t_{\text{obs}}/N$.

As additional constraint, if no bursts are observed, we require that t_{recur} is longer than the uninterrupted part of a pointing. For a 96 minute satellite orbit we estimate this as $(96 \text{ minutes}) \times \eta$. Furthermore, in our superburst selection only for the superburst on 51324.21 from 4U 1636–536 more than one burst was observed in the following month. The closest pair was separated by 17.8 hr. We use this as upper limit for t_{recur} at 24 days after the superburst onset. The combined constraints are presented in Fig. 15.

To determine the expected t_{recur} before the superbursts, we search MINBAR for the shortest time interval between two subsequent bursts that occurred at a similar level of persistent flux as the superburst. For six superbursts we find time intervals between 1.4 hr and 3.6 hr, whereas for others we find time intervals of 8.0 hr and longer. The longer t_{recur} are most likely because of a short total exposure time on a given source at the level of persistent flux of interest, and not representative of the actual t_{recur} . Indeed, the shorter time intervals are found for most of the superbursts in Fig. 14, which have the longest cumulative exposure times. Therefore, we take 1.4–3.6 hr to be the range of expected values for t_{recur} .

Comparing the expected pre-superburst t_{recur} to the limits on t_{recur} (Fig. 15), we see that $t_{\text{recur}} \leq 5.5$ hr is strongly disfavored during the first 4 days, with t_{recur} likely exceeding 12.3 hr during the first day. Therefore, these superbursts caused a substantial increase in the burst recurrence time, or possibly quenched bursts altogether. Furthermore, for most 1 day time bins the lower limit for t_{recur} is at least 0.5–1.0 hr, which disfavors bursts with shorter t_{recur} .

The strongest constraints are due to a burst from 4U 1636–536 on day 26: $0.5 \text{ hr} \leq t_{\text{recur}} \leq 1.5 \text{ hr}$. This suggests t_{recur} is back at pre-superburst values after 26 days. Only 5 days earlier, the lower limit was $t_{\text{recur}} \geq 4.2 \text{ hr}$, and on day 34 $t_{\text{recur}} \geq 3.2 \text{ hr}$: both at the upper part of the pre-superburst range. Therefore, the allowed values for t_{recur} within the pre-superburst range vary somewhat with time, which may be due to differences in the persistent flux from one superburst to the next as well as variations during the month after a given superburst.

The majority of the bursts indicated in Fig. 14 followed the superburst on MJD 51324.21 from 4U 1636–536. All those bursts have similar properties, and exhibit PRE, indicating that the Eddington limit was reached. The persistent flux was approximately 6% of the burst peak flux. The burst properties are typical for bursts from this source at that level of persistent flux. Burst properties not changing between days 15 and 26 suggest that normal bursting behavior was resumed at most two weeks after

the superburst.

4. DISCUSSION

We present one-dimensional multi-zone simulations of the neutron star envelope, where we study the effect of a superburst on a helium-rich and on a solar-composition atmosphere, where matter is accreted at a rate of $\dot{M} = 5.25 \times 10^{-9} M_{\odot} \text{yr}^{-1}$. The simulations are similar to those presented by Keek & Heger (2011) where a carbon-rich layer is build up by accretion until a superburst ignites. In the present work we replace the accretion composition shortly before the superburst to build an atmosphere of either a helium-rich or a solar composition. The results are summarized in Table 1.

We find that the hydrogen/helium-rich atmosphere changes the shock breakout and precursor peak height and duration, whereas the superburst itself does not differ substantially from models with a carbon-rich atmosphere. After the superburst all burning in the atmosphere is stable, and bursts are quenched until the envelope has cooled down from the superburst. At that point burning first becomes marginally stable, followed by weak bursts with short recurrence times. Over time, recurrence times lengthen, and the burst properties return to those from before the superburst.

4.1. Superburst

Keek & Heger (2011) found for a model with the same accretion rate and a slightly higher $Q_b = 0.13 \text{ MeV nucleon}^{-1}$ a recurrence time of 1.70 years, 33 % longer than the recurrence time found in the present study. With $Q_b = 0.1 \text{ MeV nucleon}^{-1}$ one would expect our cooler model to produce a somewhat longer recurrence time. For the models in the current paper, we use a different implementation of accretion and, most importantly, of the compressional heating from the accreted material. A further difference is the prescription used for electron conductivity.

The different phases displayed by the superburst are the same as described by Keek & Heger (2011), including the shock breakout, the precursor, and the two-component power-law decay. A difference lies in the height of the shock breakout peak and the oscillations at the start of the precursor, where super-Eddington luminosities are reached. The peak luminosity has a strong dependence on the resolution at the surface of the model (Keek & Heger 2011). The bottom of the outer zone of our models is at a column depth of $y \simeq 10^6 \text{ g cm}^{-2}$, whereas the photosphere of a neutron star is typically located at $y \simeq 1 \text{ g cm}^{-2}$, so it is likely that our simulations have not resolved this fully. A previous study also finds the shock breakout to be super-Eddington, but likewise does not fully resolve the photosphere (Weinberg & Bildsten 2007). This underlines the importance of the treatment of the outer layers during these hydrodynamic events. Whereas our non-relativistic simulations employ diffusive radiation transport, a relativistic hydrodynamic model that includes full radiation transport will be much better suited to simulate these processes in detail. Such a model will also be able to determine whether any material is lost from the neutron star during the super-Eddington luminosity phases.

4.2. Precursor

After the initial oscillations, the precursor luminosity settles at the Eddington limit, L_{Edd} , producing a plateau in the light curve. The height of the plateau is different for the three atmosphere compositions because of the dependence of L_{Edd} on the opacity, κ : $L_{\text{Edd}} \propto \kappa^{-1}$. The opacity in the neutron star photosphere is typically assumed to be dominated by Thomson scattering, which depends exclusively on the hydrogen mass-fraction. Both models He and C are devoid of hydrogen, but they reach the Eddington limit at slightly different luminosities. The opacity in the outer zones of the models continue to increase toward the surface. It is likely that the true photospheric values are not yet reached, which may explain the variations in L_{Edd} .

The precursor in model C is predominantly powered by the fallback of shock-heated material. The fluence of this precursor is about half that of the precursors in the models He and H, indicating that even in those cases fallback has a substantial contribution to the precursor, with hydrogen and helium burning accounting for the rest of the fluence.

The superburst ignited at a relatively early phase in the cycle of hydrogen/helium bursts. If it had ignited at a later phase, the respective helium-rich and solar composition columns would have been several times larger, allowing for somewhat longer precursor bursts. Note that the brightness of the precursors would not change, as it is set by the Eddington limit for the atmosphere composition. Precursor bursts that reach the Eddington limit with durations of several seconds have been observed in the few instances when the start of the superburst was observed and the data were of sufficient quality (e.g., Strohmayer & Markwardt 2002; Strohmayer & Brown 2002).

Previous models of a superburst below a helium atmosphere skipped the fallback, losing an important energy source for the precursor (Weinberg & Bildsten 2007). The shock breakout left a flat temperature profile, delaying the burst from helium burning by a thermal time scale of several seconds. The precursor of model He arrives on a dynamical time scale of $\sim 10^{-5} \text{ s}$, and is powered by both the fallback and the subsequent thermonuclear burning of helium. Furthermore, Weinberg & Bildsten 2007 argue that the thermonuclear runaway of helium is triggered either by the shock if the helium layer is sufficiently thick, or by the carbon deflagration reaching the helium layer. In our simulations the carbon deflagration does not reach that far out, and the shock does not trigger the helium burst immediately. It is rather the fallback that heats the atmosphere sufficiently to burn helium, even if the helium layer is thin (Fig. 4).

4.3. Burst Quenching

The superburst heats the atmosphere such that all subsequently accreted hydrogen and helium burn stably, and no bursts are produced. Burst quenching continues until the envelope cools down sufficiently for burning to become unstable again. Using the analytic estimate from Cumming & Macbeth (2004), one predicts for the conditions of our model a quenching time of 5.5 days for model H and 2.2 days for model He. Here it is assumed that 3α is solely responsible for the stability of thermonuclear burning. Model H, however, yields the shortest

quenching time of 1.1 days, whereas in model He bursts are quenched for 11.3 days. The latter is over five times longer than the analytic estimate, which may indicate that the approximations employed in the estimate are too strong. In contrast, we find a five times *shorter* quenching time for model H. In this case 3α is not the sole process responsible for the resumption of bursts, but the CNO breakout reaction $^{15}\text{O}(\alpha, \gamma)^{19}\text{Ne}$ plays a key role.

The importance of the $^{15}\text{O}(\alpha, \gamma)^{19}\text{Ne}$ reaction for regulating the CNO abundance in the context of X-ray bursts was stressed before by Fisker et al. (2006), and indicated as an important factor in the stability of the burning processes (Fisker et al. 2007, 2008). Our study shows its importance in determining the duration of the quenching period.

Mixing due to rotation, or a rotationally induced magnetic field, can also influence the stability of thermonuclear burning (Piro & Bildsten 2007; Keek et al. 2009). Rotation was not taken into account in this study, but could lead to a somewhat longer quenching period.

For the ignition column depth of our simulations, $y = 1.1 \times 10^{12} \text{ g cm}^{-2}$, Keek & Heger (2011) showed that the fraction of the superburst energy that is lost in neutrinos is small, whereas for ignition at larger depths neutrino losses are substantial, and the photon fluence reaches a maximum value. This maximum fluence implies that there is a maximum burst quenching time, which is longer than the values found in our simulations.

4.4. Marginally Stable Burning

When burst quenching ends, burning becomes marginally stable, producing oscillations in the light curve. This has been observed from a small number of sources as mHz quasi-periodic oscillations (mHz QPOs; Revnivtsev et al. 2001; Altamirano et al. 2008; Linares et al. 2012), and is associated with a burning mode at the transition of stable and unstable burning (Heger et al. 2007b). Using the one-zone analytic approximation from Equation (11) in Heger et al. (2007b), and substituting the values appropriate for model He ($E_\star = 594 \text{ keV nucleon}^{-1}$, $T_8 = 0.54$, $y_8 = 1.0$, and $\dot{m} = 0.3 \dot{m}_{\text{Edd}}$), one obtains the oscillation period $P_{\text{osc}} = 25$ minutes, which is close to the 20 minute period in our simulations. Marginally stable burning in model H has a period of 5 minutes, which is close to $P_{\text{osc}} = 6$ minutes predicted by the analytic approximation with $T_8 = 4.2$, $y_8 = 0.60$, and $\dot{m} = 0.3 \dot{m}_{\text{Edd}}$. The analytic estimate from Heger et al. (2007b) considers only accretion, radiative cooling, and a single thermonuclear process, the rate of which has a similar temperature dependence as the cooling rate. In the case of model He, where 3α is the single dominant thermonuclear process, this approximation seems valid. It is interesting that it also provides a good estimate of P_{osc} in model H, where the nuclear reactions proceed through a complex interplay between the 3α , hot-CNO, and CNO breakout processes.

4.5. Burst Resumption

As the envelope continues to cool, the oscillatory burning transitions into bursts. At first their fluence is relatively low and the recurrence times are short. Over time (almost four months for model He; one month for H) the burst properties regain their

pre-superburst values. The light curves of the later bursts, as well as of the pre-superburst bursts, are qualitatively similar to those reported from recent multi-zone simulations (e.g., Joss & Li 1980; Woosley et al. 2004; Fisker et al. 2008; José et al. 2010), which provide very good agreement with observed bursts (Heger et al. 2007a; in 't Zand et al. 2009; Cyburt et al. 2010).

The transition from stable burning, to bursts, via marginally stable burning (mHz QPOs), and weak bursts, has not been observed directly after a superburst. In this respect the bursting behavior of IGR J17480-2446 in the globular cluster Terzan 5 is interesting (Motta et al. 2011; Linares et al. 2011b; Chakraborty & Bhattacharyya 2011; Linares et al. 2012). During an outburst in late 2010, its accretion rate varied by more than a factor five, and it displayed a continuous transition from bright bursts to weak bursts, to mHz QPOs, and back. The changes in the burst properties are quite similar to those in model H. The weak bursts have a longer rise and recurrence times as short as a few minutes. The bursts become brighter with longer recurrence times and longer decay profiles. The decrease of the accretion rate causes the atmosphere to cool, similar to the cooling after the superburst in the models, but it also changes the burst fuel accumulation time. This is more complex than the situation in the simulations, and we cannot compare the time scale on which the changes in burst behavior take place, as it is set by the variations in the mass accretion rate, instead of the cooling time scale of the envelope.

4.6. Carbon Production and Destruction

One of the biggest challenges in superburst theory is the creation of the correct amount of carbon. Fits to superburst light curves determine the carbon mass fraction to be close to 20% (Cumming & Macbeth 2004; Cumming et al. 2006), which is the amount we adopted for our models. Models of helium bursts, or mixed hydrogen/helium bursts, however, produce less than half of that (e.g., Woosley et al. 2004). It is speculated that both bursts and stable burning of hydrogen and helium are required to produce enough carbon for superbursts. In fact, most superbursting sources exhibit this combination of burning behavior (in 't Zand et al. 2003).

Our models exhibit both burning regimes, and the next superburst will ignite at the bottom of the layer that is accreted just after the simulated superburst. Because of the relatively high temperature in the envelope after the superburst, however, most of the produced carbon burns once it is compressed to higher densities over time. Simulations over a longer time are required to determine how much carbon can survive when the envelope cools down further, and the carbon fusion reaction rate is reduced. Model He might produce a carbon-rich layer where the next superburst can ignite, whereas in model H most carbon is destroyed.

Medin & Cumming (2011) recently suggested that a larger carbon fraction can be obtained at the superburst ignition depth by separating out the carbon from heavier elements by freezing at the crust-ocean interface.

4.7. Observations after Superbursts

The detection of a burst is a certain upper limit to the quenching time. Table 2 presents the current observa-

tional upper limits on burst quenching for all known superbursts, based on the first detection of a burst following each superburst. We identify an upper limit of 15.0 days for 4U 1636–536 using the MINBAR burst catalog. This is the shortest reported value apart from the 2.2 day limit for GX 17+2, which accretes at a much higher rate than all other superbursters. 4U 1636–536 accretes hydrogen-rich material at a rate of approximately $0.1 \dot{M}_{\text{Edd}}$. The 15.0 day upper limit is well above the 1.1 day quenching time we find for model H, which has a three time higher mass accretion rate. The shortest upper limit for UCXBs, which may accrete helium-rich material, is 18.6 days for 4U 0614+091 (Kuulkers et al. 2010). Model He has a lower quenching time of $t_{\text{quench}} = 11.3$ days, but has a 30 times larger mass accretion rate.

Cumming & Macbeth (2004) estimate the dependence of t_{quench} on the accretion rate to be $t_{\text{quench}} \propto \dot{M}^{-3/4}$. Using this to correct for the differences in accretion rate between the models and the observations, model H’s $t_{\text{quench}} = 6.6$ days is still below the observational upper limit, but model He’s $t_{\text{quench}} = 28.9$ days lies above the upper limit. Considering, however, that the analytic approximation does not reproduce the results from our multi-zone models well, the accretion rate dependence here employed requires further scrutiny before conclusions can be drawn.

The two bursts following the superburst from 4U 0614+091 have the same peak flux and suggest a trend towards longer bursts at later times, just as predicted by model He.

For the hydrogen-accreting sources we combine the observations following superbursts, that are reported in MINBAR. There is a strong indication for burst quenching during the first 4 days after superbursts. A burst observed after 26 days firmly constrains the t_{recur} at a pre-superburst value. Furthermore, the lack in variation of the properties of bursts observed from 4U 1636–536 suggests that pre-superburst bursting behavior had returned already after 15 days, which is shorter than the 35 days predicted by model H. Cumming et al. (2006) derive from fits to the light curve of a different superburst from the same source an ignition column depth that is lower by a factor 0.45 compared to the ignition depth in our models. This implies a shorter cooling time scale after the superburst ($t_{\text{cool}} \propto y_{\text{ign}}^{3/4}$; Cumming & Macbeth 2004), and hence a faster return to normal bursts of 19.3 days, which is closer to what we infer from the observations.

For all but a few days, we derive $t_{\text{recur}} \geq 1$ hr. This leaves little room for the short recurrence times predicted by our models and observed from IGR J17480–2446. The majority of the observations during the first week after superbursts were, however, performed with the *BeppoSAX* WFCs, which did not have enough sensitivity to detect oscillatory behavior or weak bursts (see, e.g., Keek et al. 2010 for a comparison of the detection of weak bursts with the *RXTE* PCA and *BeppoSAX* WFCs). Alternatively, the bursting behavior after a superburst may resemble that close to the transition to stable burning observed at higher \dot{M} , when the burst rate decreases (e.g., Cornelisse et al. 2003).

Both models H and He predict a period when weak and brighter bursts alternate. This behavior has not been

observed, which is not surprising considering the short time that it is expected to take place. For model H this burning mode lasts a few hours, whereas for model He it continues for 2.3 days. It is, therefore, easiest to observe this behavior from a UCXB.

Because observations after a superburst are often few and far apart (Fig. 14), we have to combine the data for superbursts which differ by up to a factor 6 in y_{ign} (Cumming et al. 2006), and have corresponding different quenching and cooling times. A campaign of frequent and longer observations during the month following a superburst would, therefore, be very important in improving our current inability to accurately predict changes in bursting behavior. Now that *RXTE* has ceased its operations, there is no observatory available with a sufficiently large effective area and time resolution to study the mHz QPOs and weak bursts, as well as the brief superburst precursors. A future mission such as *LOFT*, that greatly improves on collecting area, will be able to make important steps forward in our understanding of thermonuclear processes on neutron stars (Feroci et al. 2011).

5. CONCLUSIONS

We create one-dimensional multi-zone models of a neutron star envelope undergoing a superburst (carbon flash), in the presence of an atmosphere of either pure helium or of solar composition. The latter is the first model of its kind. After the superburst we continue the simulations to study burst quenching as well as the return of normal Type I X-ray bursts, simulating over 900 hydrogen or helium flashes per model.

The heating of the atmosphere by fallback of shocked material generates a precursor burst that reaches the Eddington limit. Any available hydrogen or helium ignites, which extends the duration of the precursor.

After the superburst, the atmosphere is sufficiently hot for bursts to be quenched, and all hydrogen and helium to burn in a stable manner. In a pure helium layer mostly carbon is produced, and in a layer of solar composition stable *rp*-process burning creates mostly germanium and gallium. As the envelope cools down from the superburst, bursts reappear in the light curve. In the helium atmosphere this happens after 11.3 days, when the 3α -process becomes unstable. We find that in a solar composition quenching ends much sooner, after only 1.1 days. In this case it is the interplay between 3α , the hot CNO cycle, and the $^{15}\text{O}(\alpha, \gamma)^{19}\text{Ne}$ breakout reaction that leads to unstable burning.

In both models, at the transition from stable burning to unstable burning, oscillations are produced in the light curve due to marginally stable burning (Heger et al. 2007b), followed for a brief time by alternating weak and brighter bursts, which have longer and shorter recurrence times, respectively. The latter bursting mode has not been observed yet. Eventually the weak bursts disappear. In the helium atmosphere the bright bursts are immediately as bright as those before the superburst, whereas in the solar atmosphere burst peak luminosities grow as the envelope cools further. For a few days left-over helium above the burst ignition column depth burns, pausing the cooling. Afterward the burst durations and recurrence times increase back to the pre-superburst values over the course of one month for solar composition,

and four months for helium composition.

The transition from burst quenching to bursts after a superburst has not been directly observed. Using the MINBAR catalog we identify the shortest reported upper limit to the quenching time of 15.0 days for 4U 1636–536 (with the exception of GX 17+2), and we derive further constraints on the time scales for quenching and the return of bursts. The short recurrence times found by the simulations are disfavored, but not excluded. The transition between the different burning regimes that we describe exhibits, however, strong similarities with bursts observed from the transient burster IGR J17480–2446 in Terzan 5 (e.g., Linares et al. 2012).

The authors thank K. Chen for helpful discussions.

This paper uses preliminary analysis results from the Multi-INstrument Burst ARchive (MINBAR), which is supported under the Australian Academy of Science's Scientific Visits to Europe program, and the Australian Research Council's Discovery Projects and Future Fellowship funding schemes. The authors thank the International Space Science Institute in Bern for hosting an International Team on Type I X-ray bursts. L.K. is supported by the Joint Institute for Nuclear Astrophysics (JINA, grant PHY08-22648), a National Science Foundation Physics Frontier Center. A.H. acknowledges support from the DOE Program for Scientific Discovery through Advanced Computing (SciDAC, DE-FC02-09ER41618) and by the US Department of Energy under grant DE-FG02-87ER40328.

REFERENCES

- Altamirano, D., van der Klis, M., Wijnands, R., & Cumming, A. 2008, *ApJ*, 673, L35
- Asada, M., et al. 2011, *The Astronomer's Telegram*, 3760, 1
- Caughlan, G. R., & Fowler, W. A. 1988, *Atomic Data and Nuclear Data Tables*, 40, 283
- Chakraborty, M., & Bhattacharyya, S. 2011, *ApJ*, 730, L23
- Chenevez, J., et al. 2011, *The Astronomer's Telegram*, 3183, 1
- Clayton, D. D. 1968, *Principles of stellar evolution and nucleosynthesis*, ed. Clayton, D. D. (New York: McGraw-Hill, 1968)
- Cooper, R. L., Steiner, A. W., & Brown, E. F. 2009, *ApJ*, 702, 660
- Cornelisse, R., Heise, J., Kuulkers, E., Verbunt, F., & in 't Zand, J. J. M. 2000, *A&A*, 357, L21
- Cornelisse, R., et al. 2003, *A&A*, 405, 1033
- Cumming, A. 2003, *ApJ*, 595, 1077
- Cumming, A., & Bildsten, L. 2001, *ApJ*, 559, L127
- Cumming, A., & Macbeth, J. 2004, *ApJ*, 603, L37
- Cumming, A., Macbeth, J., in 't Zand, J. J. M., & Page, D. 2006, *ApJ*, 646, 429
- Cyburt, R. H., et al. 2010, *ApJS*, 189, 240
- Feroci, M., et al. 2011, *Experimental Astronomy*, 1
- Fisker, J. L., Görres, J., Wiescher, M., & Davids, B. 2006, *ApJ*, 650, 332
- Fisker, J. L., Schatz, H., & Thielemann, F.-K. 2008, *ApJS*, 174, 261
- Fisker, J. L., Tan, W., Görres, J., Wiescher, M., & Cooper, R. L. 2007, *ApJ*, 665, 637
- Galloway, D. K., Muno, M. P., Hartman, J. M., Psaltis, D., & Chakraborty, D. 2008, *ApJS*, 179, 360
- Gupta, S., Brown, E. F., Schatz, H., Möller, P., & Kratz, K.-L. 2007, *ApJ*, 662, 1188
- Haensel, P., & Zdunik, J. L. 1990, *A&A*, 227, 431
- Heger, A., Cumming, A., Galloway, D. K., & Woosley, S. E. 2007a, *ApJ*, 671, L141
- Heger, A., Cumming, A., & Woosley, S. E. 2007b, *ApJ*, 665, 1311
- Iben, Jr., I. 1975, *ApJ*, 196, 525
- in 't Zand, J., Serino, M., Kawai, N., & Heinke, C. 2011, *The Astronomer's Telegram*, 3625, 1
- in 't Zand, J. J. M., Cornelisse, R., & Cumming, A. 2004, *A&A*, 426, 257
- in 't Zand, J. J. M., Jonker, P. G., & Markwardt, C. B. 2007, *A&A*, 465, 953
- in 't Zand, J. J. M., Keek, L., Cumming, A., Heger, A., Homan, J., & Méndez, M. 2009, *A&A*, 497, 469
- in 't Zand, J. J. M., Kuulkers, E., Verbunt, F., Heise, J., & Cornelisse, R. 2003, *A&A*, 411, L487
- Itoh, N., Hayashi, H., Nishikawa, A., & Kohyama, Y. 1996, *ApJS*, 102, 411
- José, J., Moreno, F., Parikh, A., & Iliadis, C. 2010, *ApJS*, 189, 204
- Joss, P. C., & Li, F. K. 1980, *ApJ*, 238, 287
- Keek, L., Galloway, D. K., in 't Zand, J. J. M., & Heger, A. 2010, *ApJ*, 718, 292
- Keek, L., & Heger, A. 2011, *ApJ*, 743, 189
- Keek, L., & in 't Zand, J. J. M. 2008, in *Proceedings of the 7th INTEGRAL Workshop. 8 - 11 September 2008 Copenhagen, Denmark*. Online at <http://pos.sissa.it/cgi-bin/reader/conf.cgi?confid=67>, p.32
- Keek, L., in 't Zand, J. J. M., Kuulkers, E., Cumming, A., Brown, E. F., & Suzuki, M. 2008, *A&A*, 479, 177
- Keek, L., Langer, N., & in 't Zand, J. J. M. 2009, *A&A*, 502, 871
- Kuulkers, E. 2004, *Nucl. Phys. Proc. Suppl.*, 132, 466
- Kuulkers, E. 2009, *The Astronomer's Telegram*, 2140, 1
- Kuulkers, E., et al. 2010, *A&A*, 514, A65+
- , 2002, *A&A*, 382, 503
- Linares, M., Altamirano, D., Chakraborty, D., Cumming, A., & Keek, L. 2012, *ApJ*, 748, 82
- Linares, M., et al. 2011a, *The Astronomer's Telegram*, 3217, 1
- Linares, M., Chakraborty, D., & van der Klis, M. 2011b, *ApJ*, 733, L17
- Medin, Z., & Cumming, A. 2011, *ApJ*, 730, 97
- Motta, S., et al. 2011, *MNRAS*, 414, 1508
- Piro, A. L., & Bildsten, L. 2007, *ApJ*, 663, 1252
- Rauscher, T., Heger, A., Hoffman, R. D., & Woosley, S. E. 2003, *Nuclear Physics A*, 718, 463
- Revnivtsev, M., Churazov, E., Gilfanov, M., & Sunyaev, R. 2001, *A&A*, 372, 138
- Schatz, H., et al. 2001, *Physical Review Letters*, 86, 3471
- Schatz, H., Bildsten, L., Cumming, A., & Ouellette, M. 2003, *Nuclear Physics A*, 718, 247
- Serino, M., Mihara, T., Matsuoka, M., Nakahira, S., Sugizaki, M., Ueda, Y., Kawai, N., & Ueno, S. 2012, *ArXiv e-prints*
- Strohmayer, T. E., & Brown, E. F. 2002, *ApJ*, 566, 1045
- Strohmayer, T. E., & Markwardt, C. B. 2002, *ApJ*, 577, 337
- Taam, R. E., Woosley, S. E., & Lamb, D. Q. 1996, *ApJ*, 459, 271
- Wallace, R. K., & Woosley, S. E. 1981, *ApJS*, 45, 389
- Weaver, T. A., Zimmerman, G. B., & Woosley, S. E. 1978, *ApJ*, 225, 1021
- Weinberg, N. N., & Bildsten, L. 2007, *ApJ*, 670, 1291
- Weinberg, N. N., Bildsten, L., & Brown, E. F. 2006, *ApJ*, 650, L119
- Woosley, S. E., et al. 2004, *ApJS*, 151, 75
- Woosley, S. E., Heger, A., & Weaver, T. A. 2002, *Reviews of Modern Physics*, 74, 1015
- Woosley, S. E., & Weaver, T. A. 1984, in *American Institute of Physics Conference Series*, Vol. 115, AIP Conf Ser 115: *High Energy Transients in Astrophysics*, ed. S. E. Woosley, 273–297